Research Article

Bright red luminescence emission of macroporous honeycomb-like Eu^{3+} ion-doped ZnO nanoparticles developed by gel-combustion technique

E. Indrajith Naik[1] · H. S. Bhojya Naik[1] · R. Viswanath[1] · I. K. Suresh Gowda[1] · M. C. Prabhakara[2]

Received: 12 February 2020 / Accepted: 30 March 2020 / Published online: 9 April 2020

Abstract
The impact of europium (Eu^{3+}) ion doping has been outlined in improving the structure and optical properties of macroporous honeycomb-like zinc oxide (ZnO) nanoparticles, produced by the gel-combustion technique by changing the quantity of dopant. The X-ray diffraction (XRD) research verified that the hexagonal wurtzite structure of ZnO was not disturbed by Eu^{3+} substitution. Scherrer method, Scherrer plots (SP), Williamson-Hall (W–H) plots and Size-Strain plots (SSP) were used to estimate the crystallite size. Decreased crystallite size in ZnO:Eu^{3+} was noticed along with lower angle shift of XRD peaks and increased lattice parameters such as unit cell volume that can be described as replacement result of Eu^{3+} at Zn sites. Fourier transform infrared (FTIR) spectroscopy analysis confirmed the Eu^{3+} dopant by moving the peak from 474 cm^{-1} to 525 cm^{-1}. Field-emission scanning electron microscopy (FESEM) pictures verified macroporous honeycomb-like structures. UV–Visible (UV–Vis) absorption spectroscopic studies show that the ability of ZnO:Eu^{3+} nanoparticles concerning the absorption of visible light increased upon Eu^{3+} doping with a red shift compared to ZnO nanoparticles. Photoluminescence (PL) emission spectra of Eu^{3+} doped ZnO nanoparticles exhibited five intense band emissions at 579, 591, 617, 652, and 706 nm ascribed to $^5D_0 \rightarrow {}^7F_0$, $^5D_0 \rightarrow {}^7F_1$, $^5D_0 \rightarrow {}^7F_2$, $^5D_0 \rightarrow {}^7F_3$, and $^5D_0 \rightarrow {}^7F_4$ transitions of Eu^{3+} ions when excited at 465 nm wavelength, originated from intra-4f transition of Eu^{3+} ions, respectively. ZnO:Eu^{3+} nanoparticles intensified with concentration progression and revealed as nanoparticles emitting red under 465 nm excitation.

Keywords Macroporous honeycomb-like structure · ZnO · Eu^{3+} doped ZnO · X-ray diffraction · Photoluminescence

1 Introduction

Nanostructure such as CdS, SnO_2, TiO_2, ZnS, ZnO, etc. with particular morphologies has drawn growing attention in the latest years due to their technological applications and unique optical characteristics [1–5]. Zinc oxide (ZnO) is a versatility of the II–VI direct band gap semiconductor with a large 3.37 eV band gap with a large 60 meV excitonic binding energy [6–9]. The band gap and optical characteristics of ZnO nanostructure can be customized by altering the shape and size of the particles and by doping ZnO structures with separate components. The wide-band gap energy of ZnO is an adaptable host lattice for doping various components [10]. Semiconductors with rare earth (RE) doped materials are essential because of the prospective applications of such materials in optoelectronic systems, optical communication, X-ray panel display, scintillators and biological labels [11, 12]. The elevated fluorescence effectiveness of the doped nanostructure of RE metals has been of great concern in the growth of next-generation photonic instruments and

✉ H. S. Bhojya Naik, hsb_naik@rediffmail.com | [1]Department of P.G. Studies and Research in Industrial Chemistry, School of Chemical Sciences, Kuvempu University, Shankaraghatta, Karnataka 577451, India. [2]Department of P.G. Studies and Research in Industrial Chemistry, Sir. M.V. Government Science College, Bommanakatte, Shimoga, Bhadravathi, Karnataka 577302, India.

biolables. In comparison to 3d metal and non-metallic doping transitions, ZnO semiconductors with RE doped ions have been of great concern due to their f→f or f→d internal orbital transitions, which give highly intensive ultraviolet (UV) emissions, as well as visible and infrared areas [13, 14]. Moreover, the optical properties of RE ions depend mainly on the local environment or host material symmetry [15, 16]. Despite its precious technological interests, many studies on RE doped semiconductors have been conducted. The Eu^{3+} ion is a representative dopant of several distinct compounds among the RE^{3+} ions and the red release of Eu^{3+} is thoroughly explored and extensively used for light emission systems [17–21]. The luminescence characteristics of Eu^{3+} doped ZnO have become more interesting because of their enormous potential for plasma displays, fiber lasers, bio-images, solar cells, and displays in terms of emission in general [22, 23]. Trivalent europium ion is the prevailing doping agent for different compounds with a 4f emissions scheme with red emissions [24]. The issues remain for the nanotechnology community to manipulate the dopant content and to control the aspect ratio of the nanostructure. The implementation of RE^{3+} ion into ZnO was noted as not as easy as ionic radii, electric charge, and coordination number problems are involved [25, 26]. Nanorods, nanobelts, nanoneedles, nanobowls, and nanonails have been employed in many synthesis techniques. Examples of these methods are co-precipitation, sol–gel, combustion, solvothermal, microwave, etc. [21, 26–29]. An alternative is a gel-combustion reaction technique, as it does not involve intermediate composition or steps of calcinations, to make a synthesis of these Eu-doped ZnO compounds quick and cheap [30–32]. Moreover, the stoichiometric composition and crystallites size can easily be controlled which significantly impacts the luminescent properties of the Eu-doped ZnO compounds.

This article reports a systems research on the synthesis of macroporous honeycomb-like ZnO nanoparticles doped with various concentrations of Eu^{3+} ion by the gel-combustion method. Moreover, there was a comparative assessment from the X-ray diffraction (XRD) operation of the mean crystallite size of pure and doped ZnO. Williamson-Hall (W–H) plots and Size-Strain plots (SSP) estimate for the strain associated with undoped and different concentration of Eu^{3+} ion-doped ZnO nanoparticles as a result of lattice deformation. The study was extended in the form of investigating the structure and the photoluminescence (PL) characteristics of the resulting samples in detail.

2 Experimental details

2.1 Materials

Europium nitrate pentahydrate ($Eu(NO_3)_3{\cdot}5H_2O$, 99.9%), zinc nitrate hexahydrate ($Zn(NO_3)_2{\cdot}6H_2O$, 98%), and citric acid ($C_6H_8O_7$, 99.5%) as a fuel used in this work were of analytical grade were provided by Sigma-Aldrich. Distilled water was used for the preparation of stock solutions by dissolving stoichiometric quantities of metal salts.

2.2 Synthesis of macroporous honeycomb-like ZnO and Eu^{3+} doped ZnO nanoparticles

The gel-combustion technique for the design of ZnO and various concentrations of Eu^{3+} (1%, 3%, and 5%) doped ZnO nanoparticles was implemented. In a beaker, the required molar proportions of zinc nitrate, europium nitrate and, citric acid were mixed to achieve a 100 ml aqueous solution. The solution was mixed at room temperature, maintaining unity between the citric acid and the metal cation ratio. The homogeneous solution was clear and converted into a gel which was dried at 130 °C on the hot plate until the solution became viscous. Further drying makes the foam harder. The dried gel was ignited with a burning matchstick. The gel was combusted immediately and produced a fluffy porous, fine white powdery mass. The resulted materials were heat-treated at 700 °C in the tube furnace and then milled to achieve the fine powders.

2.3 Characterization

A series of techniques were adopted for the characterized such as; X-ray diffraction (XRD) using a Shimadzu diffractometer (model 6000) with CuKα radiation (λ = 1.5418 Å) in a wide range of Bragg angles (2θ) varying from 20° to 80° with a scanning rate of 2°/min at room temperature. The presence of functional groups in the samples was determined by Fourier Transform Infrared (FTIR-8400S) spectrophotometer. Field emission scanning electron microscopy (FESEM) (ZEISS EVO-50) was performed to observe the morphology of the samples. The optical absorption spectra of the samples were recorded in the range of 350–600 nm on Shimadzu-Pharmaspec-1600 UV–Visible (UV–Vis) spectrophotometer. The room temperature photoluminescence (PL) properties were measured using 325 nm monochromatized xenon lamp as the excitation source at room temperature.

3 Results and discussion

3.1 XRD analysis

Figure 1 displays XRD patterns of pure ZnO and Eu^{3+} doped ZnO nanoparticles prepared at different doping percentages (1%, 3% and, 5%). Sharp characteristic peaks were observed for all samples in the patterns matching the perfect wurtzite structure of ZnO (JCPDS data card no: 89-0510). The synthesized samples were pure ZnO without any secondary phase or impurities. In the inset of Fig. 1 when the doping concentration of Eu^{3+} ions increased, it was visible that the peak corresponding to (1 0 1) XRD patterns related to ZnO shifted to lower angles. R. Singh et al. and V. Kumar et al. also noted similar changes in ZnO with RE doping [33, 34]. In addition, a small rise in the ZnO lattice parameters was noted at doping (Table 1 and Fig. 2), which was in excellent agreement with the literature information where it was stated that this sort of outcome appeared owing to the substitution of Zn^{2+} (radius

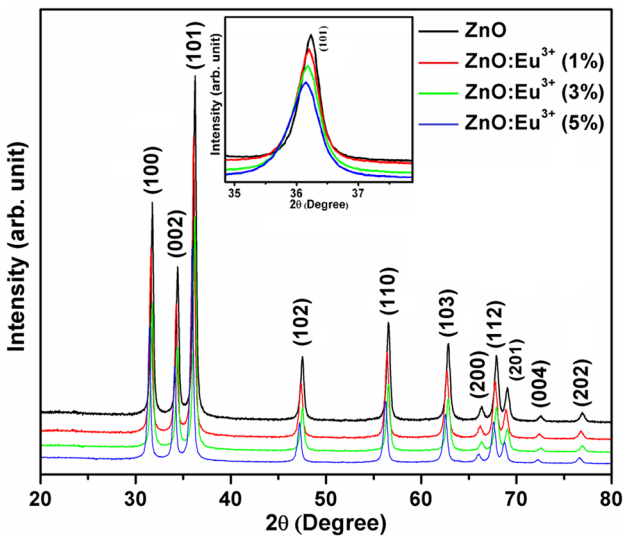

Fig. 1 XRD patterns of ZnO and distinct concentrations (1%, 3%, and 5%) of Eu^{3+} doped ZnO nanoparticles. Inset shows the peak shifting character of the plane (1 0 1) towards lower angles for Eu^{3+} doped ZnO

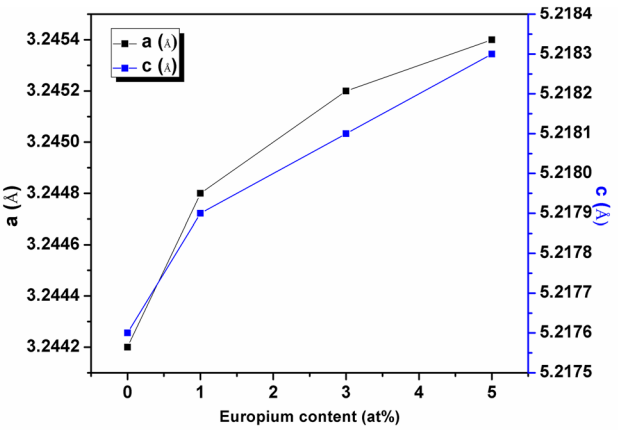

Fig. 2 Deviation with distinct levels of Eu^{3+} ions in the lattice parameters *a* and *c*

0.074 nm) with Eu^{3+} (radius 0.095 nm) in the ZnO crystal [34]. Furthermore, the peaks of diffraction of ZnO increased in width and decreased in intensity with a rise in the minimal content of Eu^{3+}, suggesting that Eu^{3+} doping inhibited the development of crystallite size. Mohanty et al. attributed this shifting peak to lattice mismatch and distortion and the strain of crystals [35].

The lattice constants for undoped and distinct concentrations of Eu^{3+} doped ZnO nanoparticles (1%, 3%, and 5%) were calculated using the following equation [36].

$$\frac{1}{d_{hkl}^2} = \frac{4}{3}\left(\frac{h^2 + hk + k^2}{a^2}\right) + \frac{l^2}{c^2} \quad (1)$$

where d_{hkl} is the interplanar spacing, *h*, *k*, *l* are miller indices, *a* and *c* are lattice constants.

The average crystallite sizes (*D*) of all the samples were calculated with the (1 0 1) peak using Scherrer formula [37].

$$D = \frac{0.9\lambda}{\beta_{hkl}\cos\theta} \quad (2)$$

where λ is the wavelength of X-ray corresponding CuKα (1.5406 Å), β_{hkl} is the full width at half maximum and θ indicates the Bragg peak position. In doped products, the

Table 1 Variation of the crystallite size, micro-strain, and the lattice constant of ZnO with different Eu^{3+} doping content

Concentration of Eu (%)	2θ of (1 0 1) peak in degree	Crystallite size (D) nm				Micro strain ($\varepsilon \times 10^{-3}$)			Lattice constant(Å)		(c/a) ratio
		Scherrer formula	SP	W–H plot	SSP	$\varepsilon = \beta_{hkl}\cos\theta/4$	W–H plot	SSP	a	c	
0	36.124	23.88	24.11	24.80	23.24	1.43	1.45	1.37	3.2442	5.2176	1.6082
1	36.044	22.22	23.51	23.90	22.17	1.54	1.57	1.40	3.2448	5.2179	1.6080
3	35.954	20.76	20.92	22.36	20.05	1.65	1.66	1.57	3.2452	5.2181	1.6079
5	35.884	19.49	21.04	20.69	19.22	1.75	1.78	1.72	3.2454	5.2183	1.6079

calculated crystallite sizes were slightly less than pure ZnO and tabulated in Table 1. This reduction in crystallite size of doped ZnO was primarily due to the creation of Eu–O–Zn on the doped product surface, which inhibits the development of crystallite size [38]. This type of inhibitory effect has also been found with different RE ions for ZnO doped [38–40]. In addition, Scherer plots (SP) were built for the ZnO and Eu^{3+} doped ZnO nanoparticles by placing *(1/cosθ)* on the x-axis and β_{hkl} *(rad)* along the y-axis as shown in Fig. 3. The crystallite size was extracted from the slope of the fit line by fitting data. $\beta_{hkl}Cos\theta$ versus *4Sinθ* was plotted for ZnO and Eu^{3+} doped ZnO nanoparticles as shown in Fig. 4, based on the Williamson-Hall (W–H) analyzes. A linear fit would achieve if plotted, $\beta_{hkl}Cos\theta$ versus *4Sinθ* for isotropic strain deformation [41]. In this work, no linear character of the W–H plot was observed. Moreover, for Eu^{3+} doped ZnO nanoparticles, the non-linear character (dispersed information spots) of the W–H model has been more influential relative to undoped ZnO. This verified that the line extension in XRD models was due to anisotropic strain in ZnO for Eu^{3+} doped ZnO nanoparticles. The linear fitting information with the W–H plot slope and intercept indicate strain and average crystallite size, respectively. Moreover, an upgraded evaluation of the size-strain variables might be extracted in isotropic instances of line extension because of an average size-strain plot (SSP) that has the benefit that less weight is given to data from high angle reflections in which the accuracy is often lower. In this estimate, it is not specified that a Lorentzian function describes the crystallite size profile and a Gaussian function describes the strain profile [42]. In Fig. 5, like to W–H methods, the term $(d_{hkl}\beta_{hkl}Cos\theta)^2$ is plotted concerning $(d^2_{hkl}\beta_{hkl}Cos\theta)$ for the all- orientation peaks of undoped and Eu^{3+} doped ZnO nanoparticles with the wurtzite hexagonal phase from $2\theta = 20°$ to 80°. The crystallite size was calculated by the slope of the linear data and the y-intercept root, which provides the strain. Table 1 sum up the average crystallite size and strain for undoped and Eu^{3+} doped ZnO

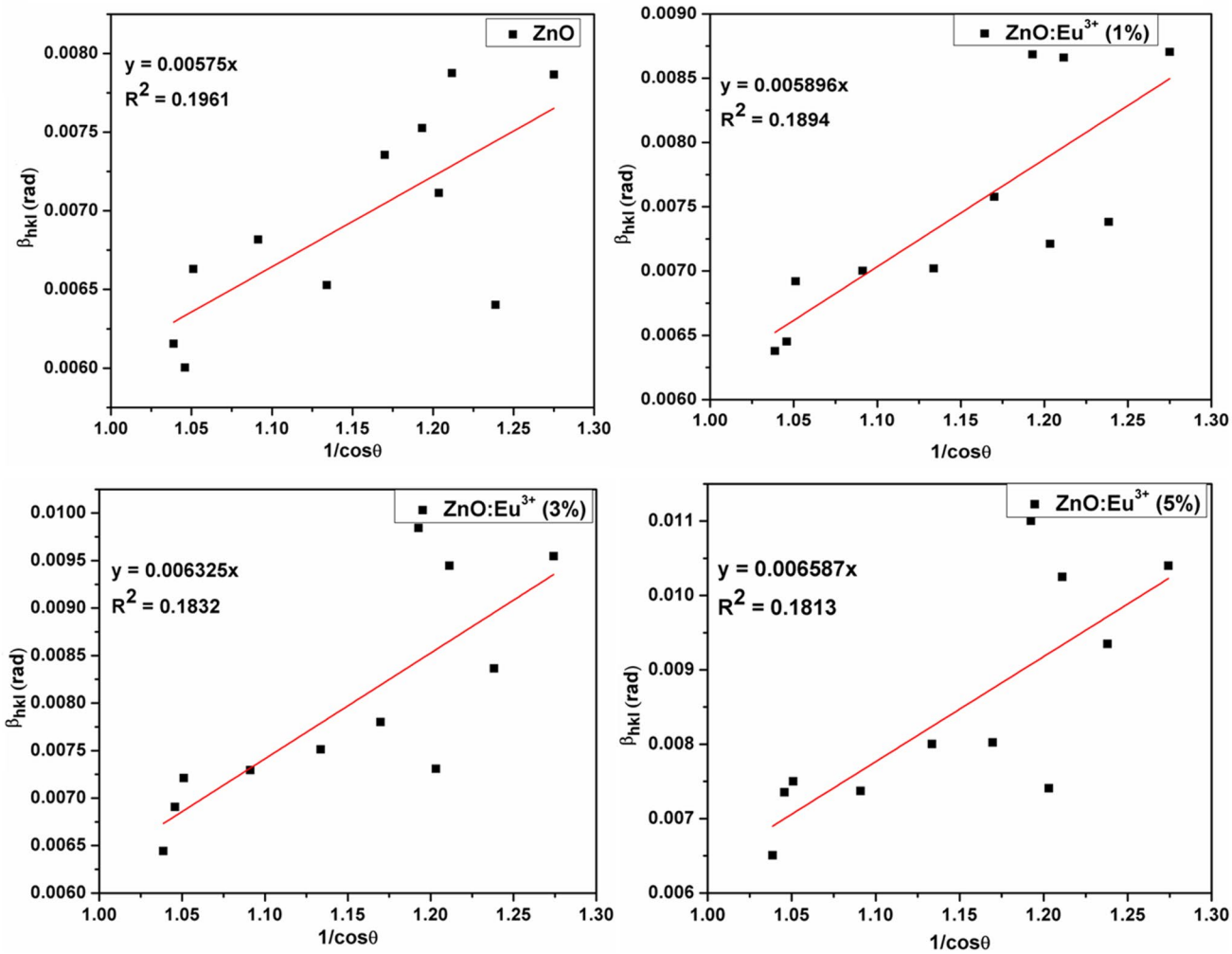

Fig. 3 Scherrer plots for estimating the size of crystallites

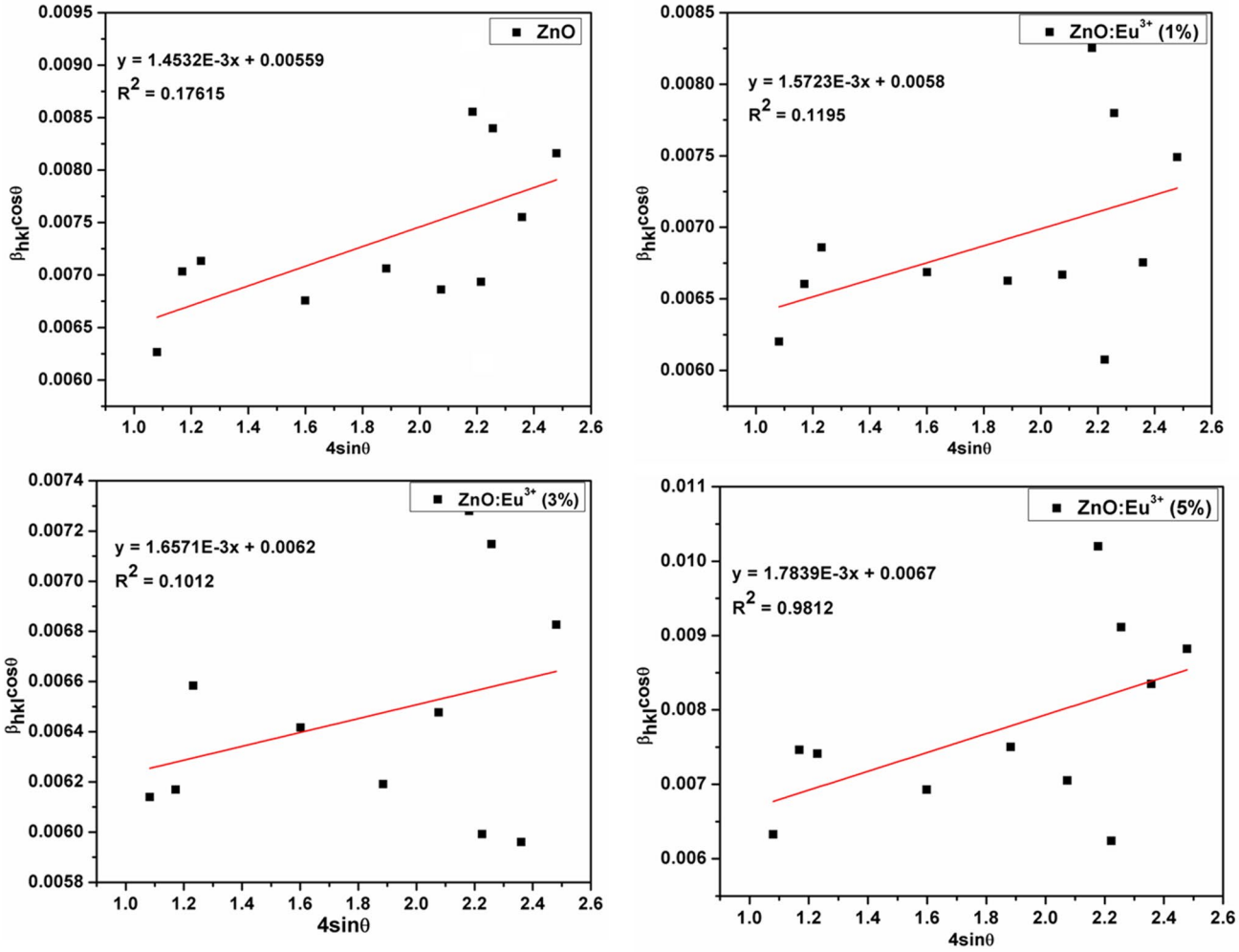

Fig. 4 XRD peak broadening of ZnO and various concentrations (1%, 3%, and 5%) of Eu^{3+} doped ZnO nanoparticles in the Williamson-Hall plots

nanoparticles. By studying the models, the findings that arose from the SSP technique were found to be more precise than the W–H because the information was placed in this design more precisely, with all elevated intensity levels affecting the linear fit. In addition, the strain of Eu^{3+} doped ZnO nanoparticles improved relative to the undoped ZnO strain. Comparable performance concerning micro-strain was also reported by K.G. Gopchandran et al. [16] upon Eu-doping with ZnO nanophosphor. This variation in the micro-strain indicates the substitution of Eu^{3+} ions into ZnO lattice.

The volume of the nanoparticles [36] was calculated using Eq. (3):

$$V = \left(\frac{4}{3}\right)\pi\left(\frac{D}{2}\right)^3 \tag{3}$$

The volume of the hexagonal unit cell [36] was predicted using Eq. (4) to compile the XRD evaluation.

$$v = 0.866a^2c \tag{4}$$

The proportion (V/v) then indicates the number of unit cells in crystallite [36] calculated with the Eq. (5):

$$n = 0.6043\left(\frac{D^3}{a^2c}\right) \tag{5}$$

This variation can be explained by a shift in the parameters *a* and *c* of the lattice.

The atomic packing fraction (APF) [43] was calculated using the Eq. (6)

$$APF = \frac{2\pi a}{3c\sqrt{3}} \tag{6}$$

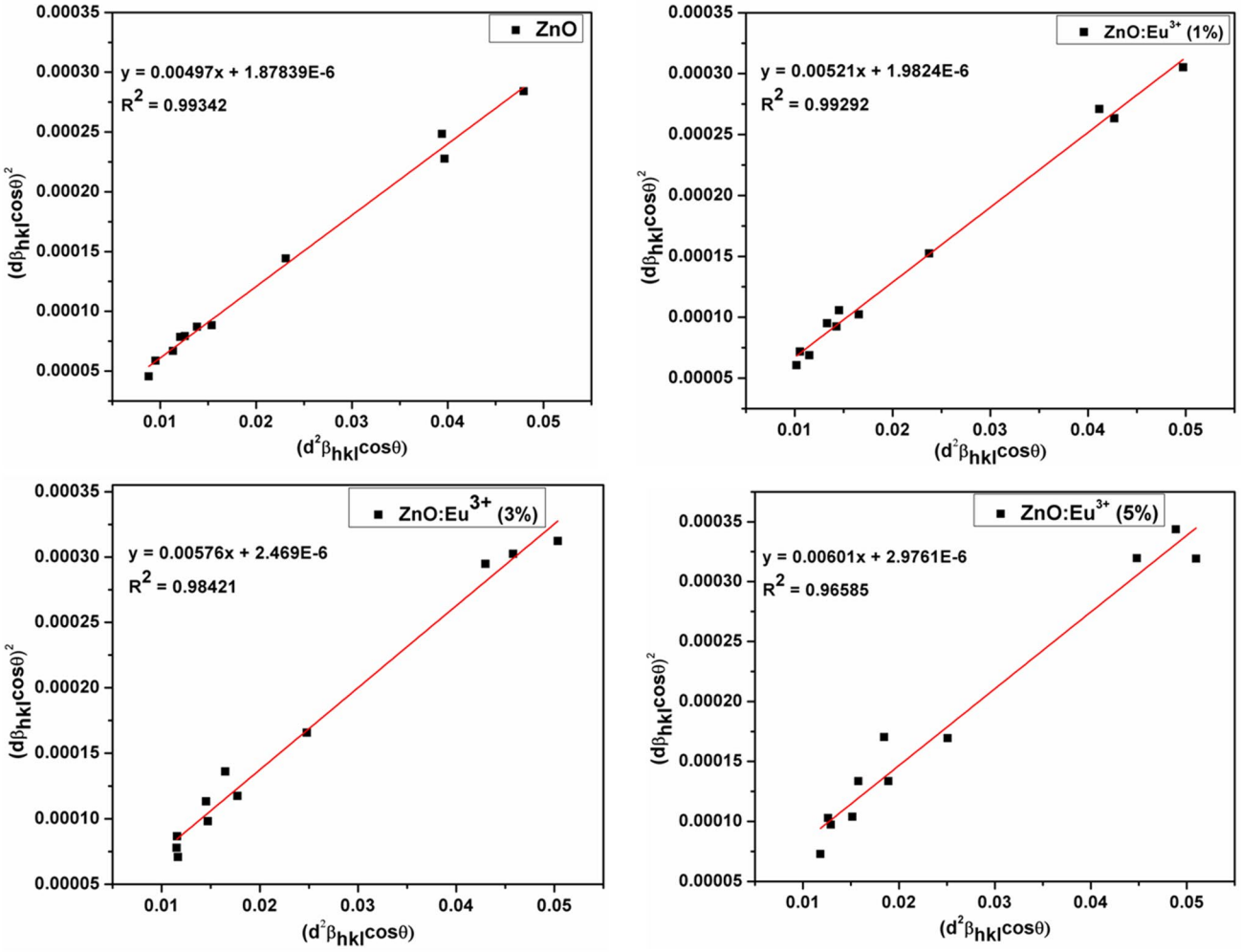

Fig. 5 Size-Strain plots to calculate the crystallite size and strain

The measured value of *APF* was approximately 75.18%, while for bulk ZnO value of *APF* is 74%. This minor change in the APF value in nanoparticles was due to the size impact. This small rise in the APF value for doped ZnO shows that dopant has been incorporated into the host lattice.

The dislocation density (δ) [36] was determined from the size of the crystallite by the Eq. (7)

$$\delta = \frac{1}{D^2} \tag{7}$$

These values were included in Table 2, indicating that δ values improved with Eu^{3+} content from 1.7528×10^{15} to 2.6316×10^{15}. This is the sign that lattice imperfection improves with reductions in crystallite size.

Similarly, micro-strain (ε) [36] was calculated using the formula.

Table 2 Additional ZnO parameters with various Eu^{3+} doping content resulting from XRD

Concentration of Eu (%)	Volume of the nano-particles V(nm)^3	Volume of the Unit cell v (Å^3)	No of Unit cells n = (V/v)	Dislocation Density ($\delta = 1/D^2$) $\times 10^{15}$	Bond Length L (Å)	APF (%)
0	7135	47.55	150.04	1.7528	1.9767	75.18
1	5744	47.57	120.73	2.0247	1.9770	75.19
3	4685	47.58	98.45	2.3200	1.9772	75.20
5	3878	47.59	81.48	2.6316	1.9773	75.20

$$(\varepsilon) = \frac{\beta_{hkl} cos\theta}{4} \quad (8)$$

In particular, this sort of ε (Table 1) variability was due to the morphology, crystallite size, and particle shape conversion.

Another method to authenticate the presence of dopant is to estimate the Zn–O bond length (L) [44]. The subsequent relationship was therefore used to assess L.

$$L = \sqrt{\left(\frac{a^2}{3} + \left(\frac{1}{2} - u\right)^2 c^2\right)} \quad (9)$$

where u is the positional parameter for wurtzite structure and is given by;

$$u = \frac{a^2}{3c^2} + 0.25 \quad (10)$$

Bond length for Zn–O was found to 1.9767 Å, and it increased (1.9773 Å) with Eu^{3+} content up to 5%, which also confirmed the replacement of Eu^{3+} ion in ZnO matrix. The variation in the volume of nanoparticles, volume of the hexagonal unit cell, number of atom per unit cell, dislocation density, APF and bond length are tabulated in Table 2.

3.2 FTIR analysis

FTIR spectra as shown in Fig. 6, details the functional properties of the synthesized powder. The Zn–O stretching mode is attributed to characteristic sharp peaks found in the range 474–525 cm^{-1}, which also confirms the development of the ZnO product [45]. The absorption at 3436 cm^{-1} was attributed to O–H stretching mode of the water molecule on the surface of the samples.[46]. The band at 2934 cm^{-1} was due to C–H stretching vibrations and the absorption peak at 2384 cm^{-1} was due to the presence of CO_2 molecules in the atmosphere [46, 47]. The band at 1564, 1035, and 759 cm^{-1} was related to the precursor materials [48, 49]. Zn–O stretching absorption bands for different content of Eu^{3+} doped ZnO nanoparticles are 474 (ZnO), 487 (1%), 512 (3%) and 525 cm^{-1} (5%). However, with the rise in Eu^{3+} content, a minute change in the position of the absorption band was noted. Faraz et al. [32] has also reported such a type of peak shift upon RE doping. This type of band shift is the indication of successful doping of Eu^{3+} ion into the Zn–O crystal structure.

3.3 FESEM

Figure 7a, b shows a low magnified and high magnified FESEM picture of the nanoparticles of 1% Eu^{3+} doped ZnO. FESEM images are clear evidence of the existence of a macroporous honeycomb-like nature of gel-combustion synthesized material. Spherical Eu^{3+} doped ZnO nanoparticles are layer by layer self-accumulating and the holes between the particles are bound. The macropores were visible in Fig. 7b and the diameter of the pore varied from 0.3 to 1.3 µm. The feasible development method of the macroporous honeycomb-like structure was observed in our case as seen in Fig. 7b. Chikkahanumantharayappa et al. [50] reported such type of morphology occurs due to nucleation, growth, and self-accumulation. Were Zn^{2+} and OH^- ions ionize first in solution after the hydrolysis process. Then the nucleation process begins between Zn^{2+} and OH^- ions [51]. The increase in reaction time outcomes in greater development and aggregation of the nucleation crystallite. Ma et al. [52] and Nagabhushana et al. [53] have also reported the formation of macropores which were generated after the calcination phase due to the evasion of gasses, which in turn leave small holes on the sample surface, which was also observed in our case. This type of macroporous structural design was acquired by the self-accumulation of nanoparticles.

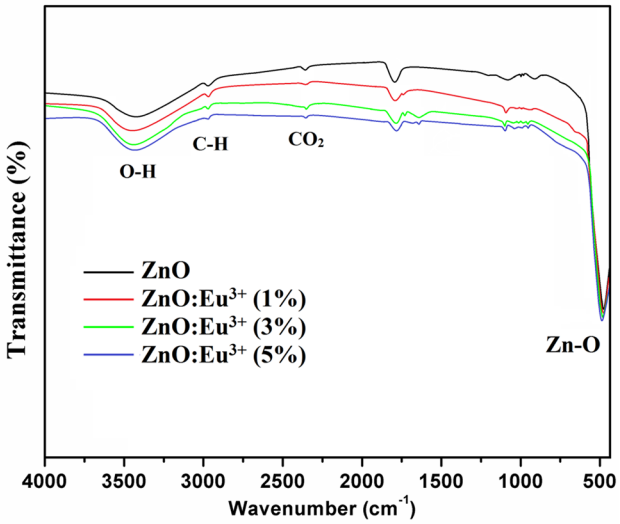

Fig. 6 FTIR spectra of different levels of Eu^{3+} doped ZnO nanoparticles (1%, 3%, and 5%)

3.4 UV–Vis spectroscopy

Figure 8 depicts the UV–Vis absorption spectra of prepared undoped and different content of Eu^{3+} doped (1%, 3%, and 5%) ZnO nanoparticles. A monotonous red shift in the absorption spectrum parallel to that of undoped ZnO nanoparticles was noted with an increase in Eu^{3+} ions concentration, which is the indication of the band gap narrowing of Eu^{3+} doped ZnO nanoparticles. This type of change in the band gap was also reported by

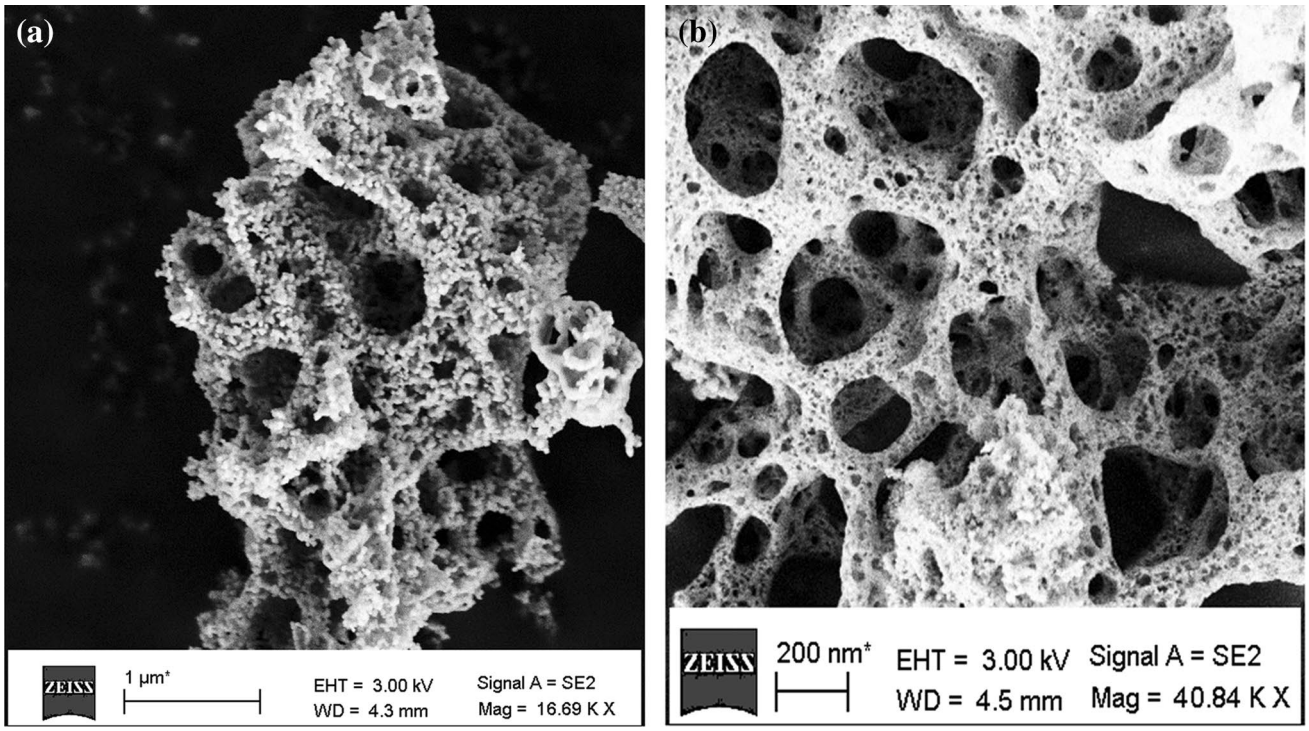

Fig. 7 SEM images of 1% Eu^{3+} doped ZnO nanoparticles with different magnification view: **a** 1 µm, **b** 200 nm

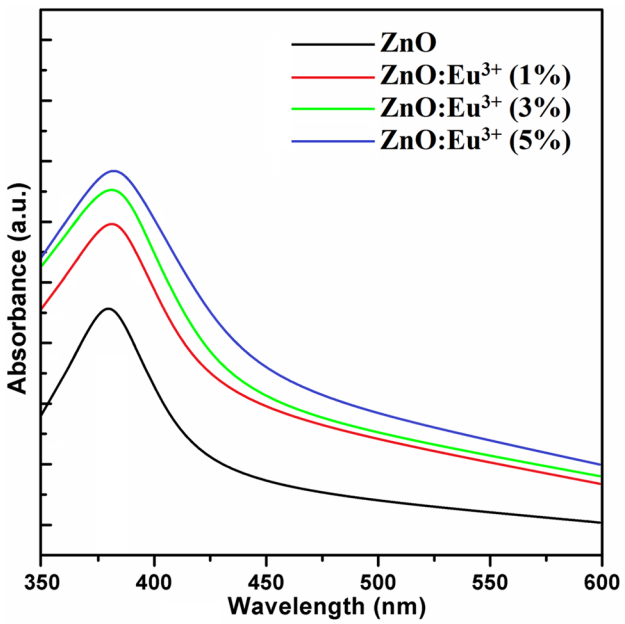

Fig. 8 UV–visible absorption spectra of pure ZnO and various Eu^{3+} doping content of (1%, 3%, and 5%) ZnO nanoparticles

Swart et al. [10] due to charge transfer between ZnO valance or conduction band concerning the 4f levels of Eu^{3+} ions. The energy gap energies were calculated by Eq. (11):

$$E_g(eV) = \frac{hc}{\lambda}(nm) \tag{11}$$

where E_g is the band gap energy (*eV*), *h* is Planck's constant (4.135667×10^{-15} *eVs*), *c* is the velocity of light (3×10^8 m/s), and λ is the wavelength (nm) of absorption onset. We then continued our research to calculate the energy gap of undoped and Eu^{3+} doped ZnO nanoparticles with the well-known Tauc's equation.

$$\alpha h\upsilon = A\left(h\vartheta - E_g\right)^n \tag{12}$$

where E_g is optical band gap, *h* is Planck's constant and υ is the frequency of incident photons, *A* is a constant called the band tailing parameter, and *n* is the index with distinct values (2, 3, 1/2, and 1/3) that are indirect allowed, indirect forbidden, direct allowed and direct forbidden transitions, respectively [54, 55]. ZnO is a semiconductor with a direct band gap, n = 1/2. The optical band gap was determined from the extrapolation of the linear portion of $(ahv)^2$ versus *hv* plot to the energy axis. The connection between $(ahv)^2$ and *hv* for ZnO and Eu^{3+} doped ZnO nanoparticles was depicted in Fig. 9. The band gap energies of the doped products were less than the pure ZnO, as indicated in Table 3. Such type of decrease in the band gap related to RE-doped ZnO compared to pure ZnO was also reported by Ntwaeaborwa et al. [24]. The findings above

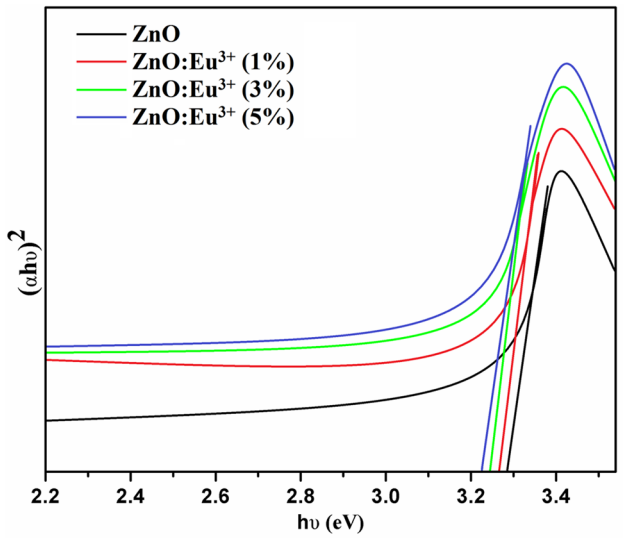

Fig. 9 The Plot of $(\alpha h\upsilon)^2$ versus hυ of ZnO and various content of (1%, 3%, and 5%) Eu^{3+} doped ZnO nanoparticles

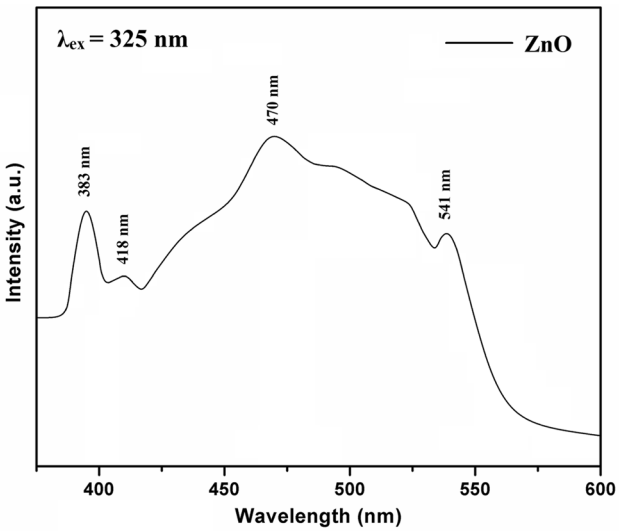

Fig. 10 Room temperature photoluminescence emission spectra of ZnO nanoparticles excited at 325 nm

showed that Eu^{3+} doped ZnO is capable of absorbing UV and visible regions of solar light. Therefore, the absorption property deduced that in sunlight photocatalysis the Eu^{3+} doped ZnO could be useful.

3.5 PL studies

Figure 10 displays the room temperature emission spectra of ZnO nanoparticles. The spectra were recorded at 325 nm wavelength excitation source using a monochromatized xenon lamp. Under the excitation of 325 nm, two bands displayed ZnO nanoparticles: (1) Band of UV emissions below 400 nm and (2) The broad visible emission band from 400 to 600 nm. The sharp UV emission band at 383 nm was associated with the near band-edge (NBE) emission of ZnO [56]. This band origin is due to the direct recombination of ZnO free excitons [57, 58]. The wide noticeable range in 400 nm to 600 nm wavelength region is due to deep-level defects in the crystal such as vacancies and oxygen and zinc interstitials [59, 60]. We discovered that our samples showed a UV emission peak at 383 nm along with three defect peaks related to violet emission close to 418 nm, blue emissions close to 470 nm and a peak connected with green emission close to 541 nm in the PL spectra. The emission peak in the violet region (418 nm) may be due to the transition from the conduction band to zinc vacancy centers [61]. Certain groups have also determined that this form of emission is linked to the transition from zinc interstitial energy levels to the valence band with non-stoichiometric ZnO [62, 63]. The observed blue emission band at 470 nm was associated with the intrinsic defects emission within the ZnO host [64]. Some groups also indicate that this blue emission arises as a result of the recombination of zinc interstitial energy level to zinc vacancy energy level [57, 65]. Oxygen vacancies and intrinsic defects can be attributed to the origin of the green band (541) [66]. The observed green emission is also due to the level of impurity corresponding to the ZnO single ionized oxygen vacancy [67]. The green emission was described by Vanheusden et al. by the transition between photoexcited holes to ionized oxygen vacancies [68]. Such type of green emission in ZnO was also reported by Zeng et al. [62] due zinc vacancies, i.e. the transition between the electrons near the conduction band and deeply trapped holes at doubly ionized oxygen vacancies.

Table 3 Calculated band gap based on the energy wave equation and Tauc plot

Concentration of Eu (%)	Absorption wavelength (λ)	E_g (eV) = hc/λ	E_g from Tauc plot
0	379.20	3.27	3.28
1	381.53	3.25	3.26
3	382.71	3.24	3.24
5	383.90	3.23	3.22

The excitation (615 nm) and emission (465 nm) spectra of ZnO:Eu^{3+} (Eu^{3+} = 1%, 3%, and 5%) nanoparticles recorded at room temperature using monochromatized xenon lamp as the excitation source as shown in Figs. 11 and 12. The excitation spectra were evaluated by tracking the wavelength of emission at 615 nm. The excitation spectra, as shown in Fig. 11, comprises of five distinctive

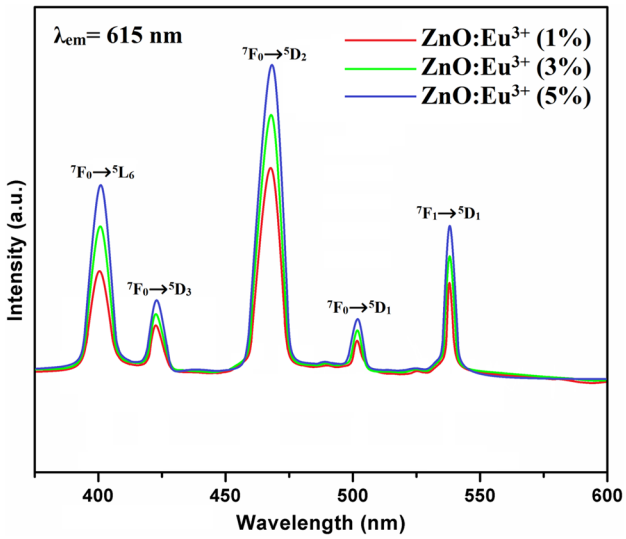

Fig. 11 Room temperature photoluminescence excitation spectra of various concentrations (1%, 3%, and 5%) of Eu^{3+} doped ZnO nanoparticles

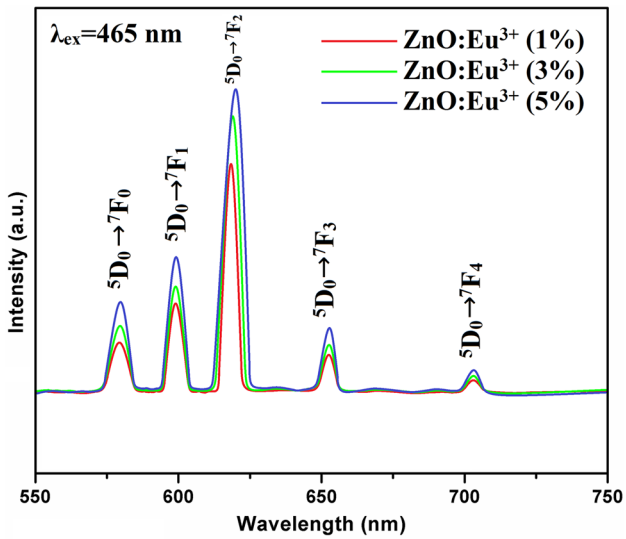

Fig. 12 Room temperature photoluminescence emission spectra of different concentrations (1%, 3%, and 5%) of Eu^{3+} doped ZnO nanoparticles

peaks at 402 ($^7F_0 \rightarrow {}^5L_6$), 416 ($^7F_0 \rightarrow {}^5D_3$), 465 ($^7F_0 \rightarrow {}^5D_2$), 501 ($^7F_0 \rightarrow {}^5D_1$), and 535 nm ($^7F_1 \rightarrow {}^5D_1$). These transitions are attributed in the ZnO lattice to intra-configurationally 4f → 4f transitions of Eu^{3+} ions [69–71]. Among these excitation peaks $^7F_0 \rightarrow {}^5D_2$ (465 nm) provides the most intense Eu^{3+} emission spectral profile. Concerning the above result, 465 nm as a pump light was adopted to produce red emissions from all Eu^{3+} doped ZnO nanoparticles.

Figure 12 shows, emission spectra (465 nm), which comprises five emission bands at 579, 591, 617, 652 and 706 nm, credited to Eu^{3+} transitions: $^5D_0 \rightarrow {}^7F_J$ (J = 0, 1, 2, 3, and 4). Nouri et al. [5] and Shi et al. [72] have also reported such type of emission bands related to Eu^{3+} ion. The first emission peak at 579 nm ($^5D_0 \rightarrow {}^7F_1$) which is related to magnetic dipole transition and its intensity hardly differs with the Eu^{3+} ion bonding environment, while the peak at 591 nm ($^5D_0 \rightarrow {}^7F_2$) is an electrically permitted transition hypersensitive to the Eu^{3+} ion coordinating environment. As reported by Cao et al. [73], the information related variation in the location of Eu^{3+} ions symmetry depends on the $^5D_0 \rightarrow {}^7F_2$ / $^5D_0 \rightarrow {}^7F_1$ intensity ratio. Based on literature related to Ramakrishna et al. [74] and Van Tran et al. [75] it can be suggested that Eu^{3+} ions occupy without inversion symmetry in our case, which was observed in the form of higher intensity related to $^5D_0 \rightarrow {}^7F_2$. These results conclude that Eu^{3+} ions are located on the host lattice without inversion symmetry. Similar results were also reported by Zamiria et al. [14], which matches in our case.

In our case, however, an increase in peak intensity was observed with the addition of doping concentration, providing electronic transitions of Eu^{3+} ions for peak intensities. Because of their charge inequality in Zn^{2+} sites, the reasons for Eu^{3+} ion incorporated deficiencies are either related to their lattice mismatch or creating an oxygen vacancy. Such types of findings were detailed by Layek et al. [41] concerning the rise in emission intensity peaks following RE ion doping. No quenching impact was seen in our situation when the concentration of dopant was increased up to 5% (Eu^{3+}). Such an impact confirms the high solubility of RE metal ions and also suggests that Eu^{3+} doping may have increased the efficiency of photoluminescence to achieve red emission nanoparticles.

As shown in Fig. 12, when the concentration of Eu^{3+} doping increased from 1 to 5%, Eu^{3+} doping had a significant impact on position $^5D_0 \rightarrow {}^7F_2$, and the transition position $^5D_0 \rightarrow {}^7F_2$ changed from 617 to 619 nm. Theoretically, the $^7F_2$ level has three crystal-field sublevels (A1, E1, E2). The A1 and E1 sublevels are nearer to the energy level reported by Lopez-Romero et al. [76] and Linare et al. [77]. As shown in Fig. 12, for Eu^{3+} doping levels of 1%, 3% and 5%, the positions of $^5D_0 \rightarrow {}^7F_2$ transition are 617 nm, 617.6 nm, and 619 nm. We think in our situation that the sublevels (A1, E1, E2) are behind the occurrence of shifting PL peak positions. We conclude that the shift in the peak position of $^5D_0 \rightarrow {}^7F_2$ was due to the enhancement of the crystal field around Eu^{3+} ions and then the emission occurred from the main emitting level $^5D_0$ to the $^7F_2$ level A1, E1 and E2 when the concentration of Eu^{3+} doping varied (1%, 3%, and 5%), respectively.

A PL assessment is used to assess the feasible mechanism for the energy transfer technique from the ZnO host

to Eu^{3+} ions. The Eu^{3+} ion peaks are the result of transitions in the PL spectra between their intra-4f levels of electron energy. When the Eu^{3+} doped ZnO nanoparticles, were excited at 465 nm, the ZnO host absorbs the excitation energy and encourages the electrons from the valence band into the ZnO host conduction band. Some of the excited electrons in the conduction band edge transit on the radioactively to surface defects of nanoparticles trapped by replaced Eu^{3+}, oxygen vacancy, zinc interstitial, then transferred to the main emission level $^5D_0$ of the Eu^{3+} ions resulting in the emission of $^5D_0 \rightarrow {}^7F_0$, $^7F_1$, $^7F_2$, $^7F_3$, and $^7F_4$ [27].

4 Conclusions

The ZnO:Eu^{3+} nanoparticles with distinct levels of Eu^{3+} ions were synthesized effectively using the gel-combustion technique. The assimilation of Eu^{3+} has created a major effect on both the shape and luminescence efficiency of ZnO:Eu^{3+} nanoparticles. It was found that the crystallite size calculated by Scherrer's technique, W–H plots, and SSP was 19.49–23.88 nm. The increase in the lattice parameters of the hexagonal unit cell was observed with increased Eu^{3+} content. This is due to the difference in Zn^{2+} and Eu^{3+} ionic radii. Analysis of the FTIR verified the existence of Eu^{3+} dopant peak change from 474 cm^{-1} to 525 cm^{-1}. FESEM studies revealed that the nanoparticle obtained was a macroporous honeycomb-like structure. Tauc relation confirmed the decreased energy gap with the increase of Eu^{3+} content. Due to distinct types of faults, broad emission spectra were noted in the observable region for undoped ZnO. The photoluminescence emission spectra of Eu^{3+} doped ZnO nanoparticles exhibited five intense emission bands at 579, 591, 616, 652, and 706 nm, which were attributed to $^5D_0 \rightarrow {}^7F_0$, $^5D_0 \rightarrow {}^7F_1$, $^5D_0 \rightarrow {}^7F_2$, $^5D_0 \rightarrow {}^7F_3$, and $^5D_0 \rightarrow {}^7F_4$ transitions of Eu^{3+} ions when excited with the 465 nm wavelength, originated from intra-4f transition of Eu^{3+} ions, respectively. The emission intensity increased with Eu^{3+} doping and the highest intensity peak was observed at 617 nm (red emission) attributable to the electric dipolar transition of $^5D_0 \rightarrow {}^7F_2$. Besides, the increase in the concentration of Eu^{3+} resulted in a PL peak position shift corresponding to transitions from the main $^5D_0$ level to the $^7F_2$ level of A1, E1, and E2. The present study shows that RE doped ZnO nanoparticles can find avenues for potential applications in optoelectronics, gas, and biosensors, photocatalysis and multicolor displays.

Acknowledgements One of the authors Indrajith Naik E. gratefully acknowledges SC/ST Cell, Kuvempu University for providing SC/ST Junior Research Fellowship and also Department of PG Studies and Research in Industrial Chemistry, Kuvempu University for providing necessary laboratory facilities. The author also acknowledges IISc (Bangalore) for SEM and other spectral data of the samples.

Compliance with ethical standards

Conflict of interest The authors declare that they have no conflict of interest.

References

1. Alrababah YM, Sheng CK, Hassan MF (2019) Influence of ammonium nitrate concentration on structural evolution and optical properties tuning of CdS nanoparticles synthesized by precipitation method. Nano-Struct Nano-Object 19:100344
2. Cheong JY, Kim C, Jung JW, Yun TG, Youn DY, Cho SH, Yoon KR, Jang HY, Song SW, Kim ID (2018) Incorporation of amorphous TiO_2 into one-dimensional SnO_2 nanostructures as superior anodes for lithium-ion batteries. J Power Sources 400:485–492
3. Dvorak F, Zazpe R, Krbal M, Sopha H, Prikryl J, Ng S, Hromadko L, Bures F, Macak JM (2019) One-dimensional anodic TiO_2 nanotubes coated by atomic layer deposition: towards advanced applications. Appl Mater Today 14:1–20
4. Viswanath R, Bhojya Naik HS, Yashavanth Kumar GS, Prashanth Kumar PN, Arun Kumar G, Praveen R (2014) EDTA-assisted hydrothermal synthesis, characterization and photoluminescent properties of Mn^{2+}-doped ZnS. J Lumin 153:446–452
5. Nouri A, Beniaiche A, Soucase BM, Guessas H, Azizi A (2017) Photoluminescence study of Eu^{3+} doped ZnO nanocolumns prepared by electrodeposition method. Optik 139:104–110
6. Kaur M, Verma NK (2013) Performance of Eu_2O_3 coated ZnO nanoparticles-based DSSC. J Mater Sci 24:3617–3623
7. Huang M, Wang S, Wan G, Zhang X, Zhang Y, Ou K, Yi L (2018) Effect of co-doped Tb^{3+} ions on electroluminescence of ZnO:Eu^{3+} LED. J Mater Sci Mater Electron 29:7213–7219
8. Perrotta A, Pilz J, Milella A, Coclite AM (2019) Opto-chemical control through thermal treatment of plasma enhancedatomic layer deposited ZnO: An in situ study. Appl Surf Sci 483:10–18
9. Belkhaoui C, Mzabi N, Smaoui H, Daniel P (2019) Enhancing the structural, optical and electrical properties of ZnO nanopowders through (Al+Mn) doping. Results Phys 12:1686–1696
10. Koao LF, Dejene FB, Kroon RE, Swart HC (2014) Effect of Eu^{3+} on the structure, morphology and optical properties of flower-like ZnO synthesized using chemical bath deposition. J Lumin 147:85–89
11. Krishna R, Haranath D, Singh SP, Chander H, Pandey AC, Kanjilal D (2007) Synthesis and improved photoluminescence of Eu:ZnO phosphor. J Mat Sci 42:10047–10051
12. Novotny M, Cek MV, Maresova E, Fitl P, Buli RJ, Pokorny P, Havlova S, Abdellaoui N, Pereira A, Hubik P, More-Chevalier J, Lancok J (2019) Optical and structural properties of ZnO: Eu thin films grown by pulsed laser deposition. Appl Surf Sci 476:271–275
13. Kumar V, Som S, Kumar V, Kumar V, Ntwaeaborwa OM, Coetsee E, Swart HC (2014) Tunable and white emission from ZnO:Tb^{3+} nanophosphors for solid state lighting applications. Chem Eng J 255:541–552
14. Zamiria R, Lemosa AF, Rebloa A, Ahangar HA, Ferreiraa JMF (2014) Effects of rare-earth (Er, La and Yb) doping on morphology and structure properties of ZnO nanostructures prepared by wet chemical method. Ceram Int 40:523–529
15. Bayan S, Mohanta D (2010) Directed growth characteristics and optoelectronic properties of Eu-doped ZnO nanorods and urchins. J Appl Phys 108:023512

16. Raji R, Kumar RG, Gopchandran KG (2019) Influence of local structure on luminescence dynamics of red emitting ZnO:Eu^{3+} nanostructures and its Judd-Ofelt analysis. J Lumin 205:179–189
17. Shinho C (2015) Synthesis and luminescent properties of Eu^{3+}-doped ZnO phosphors. J Korean Phys Soc 66:1559–1563
18. Park K, Hakeem DA, Pi JW, Jung GW (2019) Emission enhancement of Eu^{3+}-doped ZnO by adding charge compensators. J Alloys Compd 25:1040–1051
19. Liang J, Devakumar B, Sun L, Annadurai G, Wang S, Sun Q, Huang X (2019) Synthesis and photoluminescence properties of a novel high-efficiency redemitting Ca_2LuSbO_6:Eu^{3+} phosphor for WLEDs. J Lumin 214:116605
20. Yao S, Xue L, Yan Y (2011) Properties of Eu^{3+} luminescence in the monoclinic $Ba_2MgSi_2O_7$. Ceramics 55:251–255
21. Najafi M, Haratizadeh H (2015) The effect of growth conditions and morphology on photoluminescence properties of Eu-doped ZnO nanostructures. Solid State Sci 41:48–51
22. Singh LR (2015) Photoluminescence studies of ZnO, ZnO: Eu and ZnO: Eu nanoparticles covered with Y_2O3 matrix. Mater Sci Appl 6:269–278
23. Aneesh PM, Jayaraj MK (2010) Red luminescence from hydrothermally synthesized Eu-doped ZnO nanoparticles under visible excitation. Bull Mater Sci 33:227–231
24. Ntwaeaborwa OM, Mofokeng SJ, Kumar V, Kroon RE (2017) Structural, optical and photoluminescence properties of Eu^{3+} doped ZnO nanoparticle. Spectrochim Acta A 182:42–49
25. Shannon RT, Prewitt CT (1969) Effective ionic radii in oxides and fluorides. Acta Cryst 25:925–946
26. Chndrasekhar M, Nagabhushana H, Vidya YS, Anantharaju KS, Sharma SC, Premkumar HB, Prashantha SC, Prashantha BD, Prasad BD, Shivakumara C, Saraf R, Nagaswapura HP (2015) Synthesis of Eu^{3+}-activated ZnO superstructures: photoluminescence Judd-Ofelt analysis and sunlight photocatalytic properties. J Mol Catal A 409:26–41
27. Pessoni HVS, Maia LJQ, Franco A Jr (2015) Eu-doped ZnO nanoparticles prepared by the combustion reaction method: structural, photoluminescence and dielectric characterization. Mat Sci Semicond Process 30:135–141
28. Mangalam V, Pita K, Couteau C (2016) Study of energy transfer mechanism from ZnO nanocrystals to Eu^{3+} ions. Nanoscale Res Lett 11:73
29. Korake PV, Kadam AN, Garadkar KM (2014) Photocatalytic activity of Eu^{3+} doped ZnO nanorods synthesized via microwave assisted technique. J Rare Earth 32:306–313
30. Kumar DS, Ananthasivan K, Krishnan RV, Senapati A (2018) A Reaction mechanism and kinetic analysis of citrate gel-combustion synthesis of nanocrystalline urania. J Therm Anal Calorim 131:2467–2476
31. Halder R, Bandyopadhyay S (2019) Tailorable nano MgO xAl2O3 spinel compositions along line of homogeneity via gel combustion route: influence on phase evolution. Mater Chem Phys 235:121736
32. Faraz M, Naqvi FK, Shakir M, Khare N (2018) Synthesis of samarium-doped zinc oxide nanoparticles with improved photocatalytic performance and recyclability under visible light irradiation. New J Chem 42:2295–2305
33. Singh R, King A, Nayak BB (2019) Reddish emission of europium doped zinc oxide nanophosphor prepared through precipitation route using sodium borohydride. J Alloys Compd 792:1191–1199
34. Kumar V, Kumar V, Som S, Duvenhage MM, Ntwaeaborwa OM, Swart HC (2014) Effect of Eu doping on the photoluminescence properties of ZnO nanophosphors for red emission applications. Appl Surf Sci 308:419–430
35. Mohanty P, Kim B, Park J (2007) Synthesis of single crystalline europium-doped ZnO nanowires. Mater Sci Eng B 138:224–227
36. Sathya M, Pushpanathan K (2018) Synthesis and optical properties of Pb doped ZnO nanoparticles. Appl Surf Sci 449:346–357
37. Giridhar M, Bhojya Naik HS, Sudhamani CN, Viswanath R, Kenchappa R, Patil S (2019) Antibacterial activity of water soluble dye capped zinc oxide nanoparticles synthesised from waste Zn–C battery. SN Appl Sci 1:297
38. Hazra C, Sarkar S, Meesaragandla B, Mahalingam V (2013) Eu^{3+} ions as an optical probe to follow the growth of colloidal ZnO nanostructures. Dalton Trans 42:11981–11986
39. Srivastava S, Mondal A, Sahu NK, Behera SK, Nayak BB (2015) Borohydride synthesis strategy to fabricate YBO_3:Eu^{3+} nanophosphor with improved photoluminescence characteristics. RSC Adv 5:11009–11012
40. Mesaros A, Toloman D, Nasui M, Mos RB, Petrisor T, Vasile BS, Surdu VA, Perhaita I, Biris A, Pana O (2015) A valence states approach for luminescence enhancement by low dopant concentration in Eu-doped ZnO nanoparticles. J Mater Sci 50:6075–6086
41. Layek A, Banerjee S, MannaChowdhury BA (2016) A Synthesis of rare-earth doped ZnO nanorods and their defect dopant correlated enhanced visible-orange luminescence. RSC Adv 6:35892–35900
42. Tagliente MA, Massaro M (2008) Strain-driven (002) preferred orientation of ZnO nanoparticles in ion-implanted silica. Nucl Instrum Methods Phys Res B 266:1055–1061
43. Kumar P, Singh BK, Pal BN, Pandey PC (2016) Correlation between structural, optical and magnetic properties of Mn-doped ZnO. Appl Phys A 122:1–12
44. Bindu P, Thomas S (2014) Estimation of lattice strain in ZnO nanoparticles: X-ray peak profile analysis. J Theor Appl Phys 8:123–134
45. Dhanuskodi S, Rajeswari P, Sreekanth P, Philip R (2015) Ensemble effect of intrinsic defects and Mn ions on the enhancement of third order nonlinearity of ZnO nanoparticles. Nanotech 26:275702
46. Fabbiyola S, Sailaja V, Kennedy LJ, Bououdina M, Vijaya JJ (2017) Optical and magnetic properties of Ni-doped ZnO nanoparticles. J Alloys Compd 694:522–531
47. Faraz M, Shakir M, Khare N (2017) Highly sensitive and selective detection of picric acid using a one pot biomolecule inspired polyindole/CdS nanocomposite. New J Chem 41:5784–5793
48. Khan I, Khan S, Nongjai R, Ahmed H, Khan W (2013) Structural and optical properties of gel-combustion synthesized Zr doped ZnO nanoparticles. Opt Mater 35:1189–1193
49. Sohail A, Faraz M, Arif H, Bhat SA, Siddiqui AA, Bano B (2017) Deciphering the interaction of bovine heart cystatin with ZnO nanoparticles: Spectroscopic and thermodynamic approach. Int J Biol Macromol 95:1056–1063
50. Basavalingiah KR, Harishkumar S, Udayabhanu NG, Rangappa D, Chikkahanumantharayappa (2019) Highly porous, honeycomb like Ag–ZnO nanomaterials for enhanced photocatalytic and photoluminescence studies: green synthesis using Azadirachta indica gum. SN Appl Sci 1:935
51. Wang Y, Zhao X, Duan L, Wang F, Niu H, Guo W, Ali A (2015) Structure, luminescence and photocatalytic activity of Mg-doped ZnO nanoparticles prepared by auto combustion method. Mater Sci Semicond Process 29:372–379
52. Lou J, Ma SY, Cheng L, Song HS, Li WQ (2015) Facile fabrication and enhanced acetic acid sensing properties of honeycomb-like porous ZnO. Mater Lett 138:100–103
53. Reddy AJ, Kokila MK, Nagabhushana H, Chakradhar RPS, Shivakumara C, Rao JL, Nagabhushana BM (2011) Structural, optical and EPR studies on ZnO: Cu nanopowders prepared via low-temperature solution combustion synthesis. J Alloys Compd 509:5349–5355

54. Tauc J (1968) Optical properties and electronic structure of amorphous ge and si. Mater Res Bull 3:37–46
55. Tauc J, Grigorovici R, Vancu A (1966) Optical properties and electronic structure of amorphous germanium. Phys Stat Sol 15:627–637
56. Raji R, Gopchandran KG (2017) ZnO nanostructures with tunable visible luminescence: Effects of kinetics of chemical reduction and annealing. J Sci Adv Mat Dev 2:51–58
57. Sahu D, Panda NR, Acharya BS (2017) Effect of Gd doping on structure and photoluminescence properties of ZnO nanocrystals. Mater Res Exp 4:114001
58. Sahu D, Panda NR, Acharya BS, Panda AK (2014) Enhanced UV absorbance and photoluminescence properties of ultrasound assisted synthesized gold doped ZnO nanorods. Opt Mater 36:1402–1407
59. Layek A, De S, Thorat R, Chowdhury A (2011) Spectrally resolved photoluminescence imaging of ZnO nanocrystals at single-particle levels. J Phys Chem Lett 2:1241–1247
60. Panigrahy B, Aslam M, Misra DS, Ghosh M, Bahadur D (2010) Defect-related emissions and magnetization properties of ZnO nanorods. Adv Funct Mater 20:1161–1165
61. Das D, Panda NR, Sahu D (2019) Photoluminescence and photocatalytic properties of europium doped ZnO nanoparticles. Appl Surf Sci 495:666–674
62. Zeng BH, Duan G, Li Y, Yang S, Xu X, Cai W (2010) Blue luminescence of ZnO nanoparticles based on non-equilibrium processes: Defect origins and emission controls. Adv Funct Mater 20:561–572
63. Zeng H, Cai W, Hu J, Duan G, Liu P, Li Y (2006) Violet photoluminescence from shell layer of Zn/ZnO core-shell nanoparticles induced by laser ablation. Appl Phys Lett 88:171910
64. Zhong M, Shan G, Li Y, Wang G, Liu Y (2007) Synthesis and luminescence properties of Eu^{3+}-doped ZnO nanocrystals by a hydrothermal process. Mater Chem Phys 106:305–309
65. Tatsumi T, Fujita M, Kawamoto N, Sasajima M, Horikoshi Y (2004) Intrinsic Defects in ZnO films grown by molecular beam epitaxy. Jpn J Appl Phys 43:2602–2606
66. Gong Y, Andelman T, Neumark GF, O'Brien S, Kuskovsky IL (2007) Origin of defect-related green emission from ZnO nanoparticles: effect of surface modification. Nanoscale Res Lett 2:297–302
67. Gupta H, Singh J, Dutt RN, Ojha S, Kar S, Kumar R, Reddy VR, Singh F (2019) Defect-induced photoluminescence from gallium doped zinc oxide thin films: influence of doping and energetic ion irradiation. Phys Chem Chem Phys 21:15019–15029
68. Vanheusden K, Warren WL, Seager CH, Tallant DR, Voigt JA, Gnade BE (1996) Mechanisms behind green photoluminescence in ZnO phosphor powders. J Appl Phys 79:7983–7990
69. Sajna MS, Gopi S, Prakashan VP, Sanu MS, Joseph C, Biju PR, Unnikrishnan NV (2017) Spectroscopic investigations and phonon side band analysis of Eu^{3+}-doped multicomponent tellurite glasses. Opt Mater 70:31–40
70. Babu BC, Buddhudu S (2014) Emission spectra of Tb^{3+}:Zn_2SiO_4 and Eu^{3+}:Zn_2SiO_4 sol-gel powder phosphors. J Spectrosc Dyn 4:1–8
71. Qiao X, Cheng Y, Qin L, Qin C, Qin P, Cai S, Il K, Jin Seo H (2014) Coprecipitation synthesis, structure and photoluminescence properties of Eu^{3+} doped sodium barium borate. J Alloys Compd 617:946–951
72. Han B, Li P, Zhang J, Zhang J, Xue Y, Suo X, Huang Q, Feng Y, Shi H (2015) First observation of the emission from ^5D_J (J = 1, 2, 3) energy levels of Eu^{3+} in $Bi_4O_3(BO_3)(PO_4)$:Eu^{3+} phosphor. Mater Lett 158:208–210
73. Wang M, Huang C, Huang Z, Guo W, Huang J, He H, Wang H, Cao Y, Liu Q, Liang J (2009) Synthesis and photoluminescence of Eu-doped ZnO microrods prepared by hydrothermal method. Opt Mater 31:1502–1505
74. Ramakrishna PV, Murthy DBRK, Sastry DL (2014) White-light emitting Eu^{3+} co-doped ZnO/Zn_2SiO_4:Mn^{2+} composite microphosphor. Mol Biomol Spectrosc 125:234–238
75. Van Tran TT, Dung Cao TM, Lam QV, Le VH (2017) Emission of Eu^{3+} in SiO_2-ZnO glass and SiO_2-SnO_2 glass-ceramic: correlation between structure and optical properties of Eu^{3+} ions. J Non-Cryst Solids 459:57–62
76. Romero SL, Quiroz-Jimenez MJ, Garcia MH, Castillo AA (2014) Bright red luminescence and structural properties of Eu^{3+} ion doped ZnO by solution combustion technique. World J Condens Matter Phys 4:227–234
77. Linares C (1968) Spectre optique et champ cristallin de l'ion Eu^{3+} dans quelques oxydes de terres rares. J Phys 29:917–925